The Gutenberg-Richter and similar laws and their relation with numerical and experimental laboratory results

Jorge Daniel Riera
Universidade Federal do Rio Grande do Sul, UFRGS, DECIV/ PPGEC, Brazil

Ignacio Iturrioz
Universidade Federal do Rio Grande do Sul, UFRGS, DEMEC / PROMEC, Brazil

SUMMARY:

A justification of the ubiquitous Gutenberg-Richter (*GR*) law on physical grounds has been sought with partial success. On the other hand, during compression tests on concrete or rock specimens, the statistical analysis of acoustic emission (*AE*) signals emerging from growing microcraks constitutes an effective damage assessment criterion. It has been observed that these signals amplitudes are distributed according to the *GR* law and characterized through its *b*-value, which decreases systematically with damage growth. Using the Discrete Element Method (*DEM*), relations between *AE* signals magnitude and energy release in each localized rupture were analyzed. The results are compatible with the *GR* energy-magnitude relation, as well as with most proposed probability distributions of magnitudes. These results suggest that some features of the probability distribution of earthquake magnitudes may be correlated with the evolution of the damage process for the source under consideration and that these features may be assessed using numerical models.

Keywords: Gutenberg-Richter Law, b-value, Magnitude Distribution, Accoustic Emision, Rupture of solids

1. INTRODUCTION

A justification of the ubiquitous Gutenberg-Richter (*GR*) law on physical grounds has been sought in Seismology with partial success. On the other hand, during laboratory compression tests on concrete or rock specimens, the statistical analysis of acoustic emission (*AE*) signals emerging from growing microcracks has recently shown that the signals amplitudes are distributed according to the *GR* law and characterized through its *b*-value, which decreases systematically with damage growth. The authors review available field and laboratory evidence on the subjects, before presenting numerical simulations of the latter, obtained by means of the Discrete Element Method (*DEM*). These results suggest that some features of the probability distribution of earthquake magnitudes may be correlated with the evolution of the damage process for the source under consideration and that these features may be assessed using numerical models.

2. MAGNITUDE - FREQUENCY RELATION

The well-known *GR* expression for the relative frequency of seismic events larger than magnitude M_S suggested by Gutenberg and Richter (1954), has proved to be applicable in a surprising variety of geological and geographical locations:

$$Log_{10}\, N\,(\,M_S\,) = a - b\,M_S \qquad (2.1)$$

The linear relation (2.1) presents a generally satisfactory fit to available global data, both for clearly identifiable seismogenic sources as well as for difused seismicity regions. From equation (2.1) it follows that the probability of occurrence of an event of magnitude equal or larger than M_S is given by:

$$\text{Prob}\,[M_S \geq m] = \exp\,(-\beta\, m\,) \qquad (2.2)$$

$$\beta = b \ln 10 \tag{2.3}$$

Thus, the *GR* frequency relation implies an exponential distribution of seismic magnitudes. In real situations, an upper limit is often imposed, defining the largest earthquake m_{max} that is considered possible due to a specific seismogenic source. To account for the associated uncertainty in m_{max} , a probability distribution may be adopted, rather than a determined value. Similarly, a lower bound m_{min} may also be specified, which is in this case associated to the smallest event of engineering interest. In the presence of bounds, the relation between the yearly number N of seismic events larger than m results:

$$N(m) = \nu_{min} \{ exp[-\beta (m - m_{min})] - exp[-\beta (m_{max} - m_{min})] / [1 - exp[-\beta (m_{max} - m_{min})]]\} \tag{2.4}$$

In which β is also defined by equation (2.3) and ν_{min} denotes the number of events larger than m_{min} per year. In order to improve the fit of the magnitude-frequency relation to observed data, other models were suggested in the literature:

$$Log\ N(M_S) = a + b M_S - c M_S^2 \tag{2.5}$$

$$Log\ N(M_S) = a - b M_S + Log(c - M_S) \tag{2.6}$$

$$Log\ N(Log M_S) = a + b Log M_S - c (Log M_S)^2 \tag{2.7}$$

In equation (2.5) it is assumed that M_S is characterized by a log-normal probability distribution. Esteva (1976) argues that *G-R* equation (2.1) does not satisfactorily fit data that contain magnitudes above M_S= 7, proposing for such cases a double exponential function. A revision of statistical methods to estimate the *b*-coefficient in GR law as well as its associated uncertainty is due to Marzocchi and Sandri (2003).

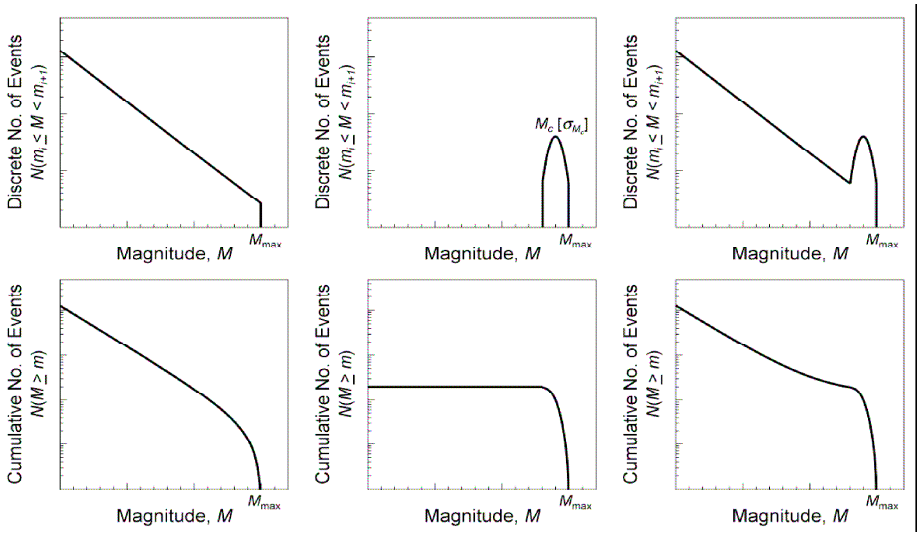

Figura 2.1. Typical recurrence relations, not-cumulative (above) and cumulative (below). *From left to right*: Gutenberg-Richter model, maximum magnitude model and characteristic earthquake model (Bommer and Stafford, 2008).

A single function, based on the hypothesis that the *GR* law is valid for *low and for high magnitudes, but with different parameters in both regions*, with a smooth transition defined by the logistic function $f(M_S)$, has been recently employed by Riera (2009):

$$Log\ N\ (\ M_S\ ) = [(a_1 - b_1\ M_S)\ \ f(M_S) + [(a_2 - b_2\ M_S)\ [1\text{-}f(M_S)] \qquad (2.8)$$

$$f(M_S) = \ exp[-(M_S - M_C)/s]\ /\{\ 1+ exp[-(M_S - M_C)/s]\ \} \qquad (2.9)$$

In addition to the doubly truncated *GR* law given by equation (2.4), which is assumed applicable to small magnitude events, its combination with the so-called *Characteristic Earthquake* model, has also been suggested for cases in which a fault generates large earthquakes at intervals that are shorter than predictions based on the observation of small events. (Schwartz and Coppersmith, 1984; Youngs and Coppersmith, 1985; Wesnousky, 1994). Note that in the group of models reviewed by Bommer & Stafford (2008), the models described by equations (2.5) to (2.9) are not mentioned.

3. BASIC RELATIONS BETWEEN MAGNITUDE MEASURES AND FAULT PROPERTIES

According to the Elastic Dislocation Theory, seismic events are due to shear failures, the seimic moment M_o being defined as (Abe, 1975):

$$M_o = \mu\ D\ A \qquad (3.1)$$

In eq. (3.1) D denotes the mean displacement on the failure plane. Moreover, eq.(3.2) relates the seismic moment to the rupture área A and the average stress drop $\Delta\tau$:

$$M_o = C\ A^{3/2}\ \Delta\tau \qquad (3.2)$$

The numerical coefficient C depends on the shape of the rupture surface, on the distribuition of applied stresses and on the degree of anisotropy of the medium. Typically, C varies between 0.6 and 0.75, its actual value being different for each seismic event. In the static approach, the parameters that decribe the fault mechanism are its length L and width B, the shear modulus of the material μ and the seismic moment M_o , which are related by simple expressions. The mean stress $E(\tau)$ is needed to assess the change in strain energy ΔW caused by a seismic event. A fraction of this energy ΔW, known in Seismology as *seismic efficiency*, is irradiated in the form of seismic waves. The irradiated energy may also be quantified in terms of the mean stress drop $\Delta\tau$.

Basic relations between these parameters were given by Kanamori and Anderson (1975). The Moment Magnitude scale M_w was proposed by Hanks and Kanamori (1979) and defined as:

$$M_w = ⅔\ log_{10}\ M_o - 10.7 \qquad (3.3)$$

In which M_o is expressed in dyne×cm (10^{-7} Nm). Expression (3.3) has been adopted by the USGS for large US earthquakes since 2002. Expressing A and $\Delta\tau$ metric units and substituting eq.(3.2) into (3.3), it follows that:

$$M_w = log_{10} A + ⅔\ log_{10}\ \Delta\tau - 6{,}147 \qquad (3.4)$$

While it is obvious that $\Delta\tau$ cannot exceed the shear (or frictional) strengths of rock, no similar physical restriction can normally be imposed on the rupture area A. Otherwise it would be easy to establish the upper bound M_{max} indicated in Fig. (2.1). However, this is not the case in laboratory specimens, as will be discussed in Section 5.

4. JUSTIFICATION OF FREQUENCY RELATIONS ON PHYSICAL GROUNDS

Numerous attempts have been made, with limited success, to explain on physical principles the satisfactory fit of *GR* or similar relations to observed seismic data. The subject still constitutes a promising area of research. Scholz (1968) attempted to relate the process of microfracturing in rocks observed in laboratory specimens with the frequency distribution of earthquakes. Bak and Tang (1989), following a theoretical approach, interpret the Gutenberg and Richter relation as a manifestation of *self-organized criticality* – (SOC), which has its fundaments in the Theory of Fractals. The approach was extended by Ito and Matsuzaki (1990), who develop a model to explain some seemingly fractal properties of seismic events, such as the potential distribution function of the size of earthquakes.

Carpinteri *et al* (2009) examined recently, employing accousting emission (*AE*) techniques, the applicability of *GR* relation in the ruptures process of concrete samples in laboratory tests in which they detected an evolution of the value of the b-coefficient from 1.5 to 1, as the system passes from the critical pre-failure state to final collapse.

This decrease of the b-coefficient, also observed in laboratory samples by Scholz (1968, 2002), does not reproduce the *increase* in earthquake frequency vs. magnitude relations for entire regions, in which for lower magnitudes the slope b_1 in eq. (2.9) is always smaller than b_2. In fact , Scholz (2002) argues that from the size distribution of subfaults it follows that $b_1 = ⅔$, while $b_2 = 1$, values that present a surprising universality. On the other hand, the coefficient $b = ⅔$ that would satisfactorily fit data for small earthquakes, say with $M_S < 3$, occurred along a single fault, would be likely to underestimate the magnitude of a large earthquake from the same seismogenic source.

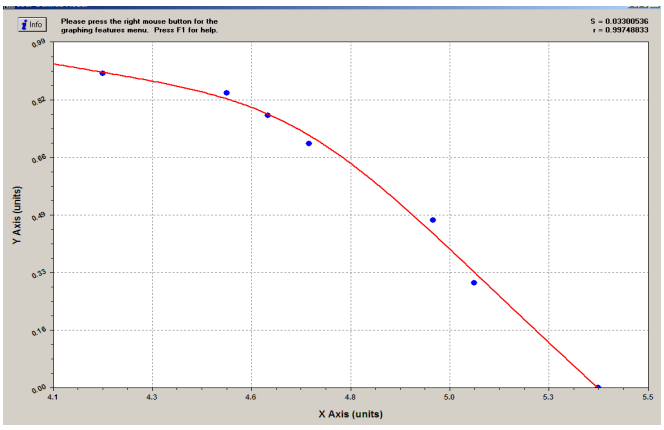

Figure 4.1. Fit of eqs. 2.9 to data from various sources in 70600km^2 low seismicity area in a stable continental region (SCR), in which $M_C = 4.7$ and $s = 0.2$, $b_1 = 0.2603$ and $b_2 = 1.0227$.

Figure 4.1 shows a typical example of data for various sources in a 70600km^2 low seismicity area in a stable continental region (SCR), in which $M_C = 4.7$, $s = 0.2$, $b_1 = 0.2603$ and $b_2 = 1.0227$. As is often the case, the slope b in the high magnitudes region is close to 1, although the slope in the low magnitude region is about a third of the theoretical value $b_1 = ⅔$ previously indicated. Almost invariably, seismic data leads to curves characterized by *increasing* negative slopes as the magnitude increases.

5. NUMERICAL AND EXPERIMENTAL RESULTS RELATED TO ACCOUSTIC EMISSION

In the following, illustrative experimental results as well as numerical simulations of laboratory tests aimed at the determination of the *b* value on small scale rock or concrete samples are described in detail. Updated information on the fundaments and performance of the lattice formulation of the Discrete Element Method (DEM) proposed by Riera (1984), which was employed in the numerical analyses reported below, may be found in Kosteski *et al* (2011). The study will focus on Accoustic Emmission (AE) tests reported by Carpinteri *et al* (2009). The first test consists of a 160×160×500mm concrete prism subjected to uniaxial compression. The laboratory specimen was modeled by means of a 27×27×86 DEM cubic modules array, with the boundary conditions shown in Figure 5.3b. The parameters adopted in the DEM model are: Young´s modulus of the material E=9.0 GPa, mass density ρ=2500Kg/m2, mean value of the material toughness $\mu(G_f)$=560N/m and the linear elastic limit strain $\varepsilon_p=2.4\times10^{-4}$. The random nature of the material is taken into account by defining the material toughness as a random field with a coefficient of variation CV= 0.5. The value of the concrete modulus E=9GPa was adopted on account of the fact that the test sample was subjected during 48 hours to a uniform compression load of 1300 kN, then unloaded. During the ensuing test the damaged specimen was reloaded up to its final collapse, while monitored by *AE* sensors. Figure 5.3b shows the location of the *AE* sensor, at which accelerations in the direction normal to the specimen surface were computed employing the DEM.

The second example consists of a three point bending test. The concrete specimen dimensions were (80×150×700mm) with a 30mm pre-fissure length in the middle. The *AE* sensor was mounted as indicated by the gray box in Fig. 5.4b. Material properties were $E=35GPa$, ρ=2500Kg/m2, mean value of the specific fracture energy – material toughness – $\mu(G_f)$=130N/m and linear elastic limit strain $\varepsilon_p=6.4\times10^{-5}$. Additional details concerning the experiments are given by Carpinteri *et al* (2009, 2009b). Again, the non-homogeneous nature of concrete is taken into account in the numerical simulations by assuming that toughness is a 3D random field with CV= 0.25. The applied displacement rates on DEM models, solved by explicit numerical integration in the time domain, were reduced until no inertial effects could be detected in the output.

Figure 5.1 shows the load vs. time diagrams measured in the experiments and determined herein by numerical simulation. The peak loads and the areas under the curves are similar in both examples, except for the loss of linearity of the experimental curve for uniaxial compression near the peak load, which suggests that perceptible damage occurred before the peak, effect that is not observed in the numerical analysis. The load vs. time diagrams of both controlled displacement tests are quite different: in the compression test an explosive collapse occurs, while in the three point bending test a softening branch after the peak load is reached can be seen. Figure 5.2 shows the normalized energy balance in both tests determined by numerical simulation. In the uniaxial compression test, 95% of the external work is available in the form of elastic energy when the final collapse occurs, resulting in an explosive failure. On the other hand, in the three point bending test the external work is smoothly dissipated during the entire process and the available potential energy at the end of the test is not sufficient to produce an explosive collapse. Note that $E_{max}=U_e+U_k+U_d$ at t*. In both examples, due to the slow rate of loading, the kinetic energy remains low throughout most of the test, although when collapse occurs under uniaxial compression, there is a sudden shift of elastic energy to kinetic energy. The final rupture configurations observed in the experimental setup and predicted numerically can be seen for the uniaxial compression test in Figure 5.3 and for the Three Point Bend test in Figure 5.4.

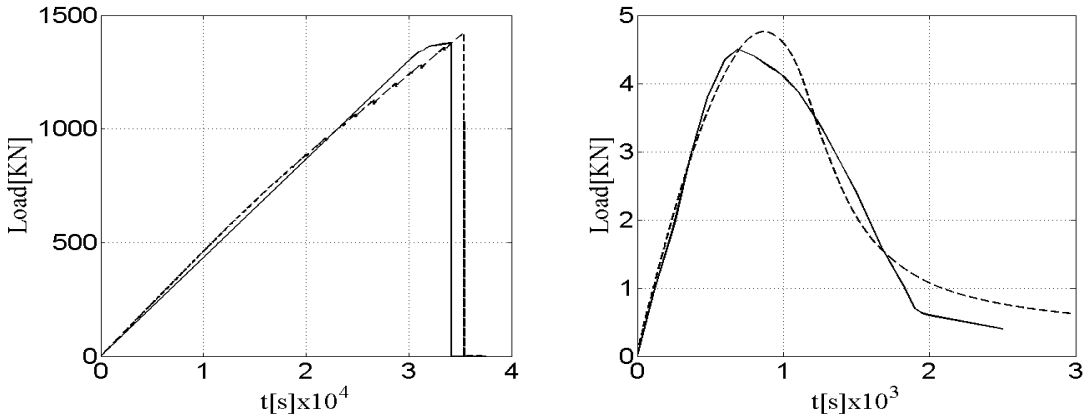

Figure 5.1. Load vs. time functions: experimental (full lines) and numerical (dashed lines): (a) Uniaxial compression test, (b) The three point bending test.

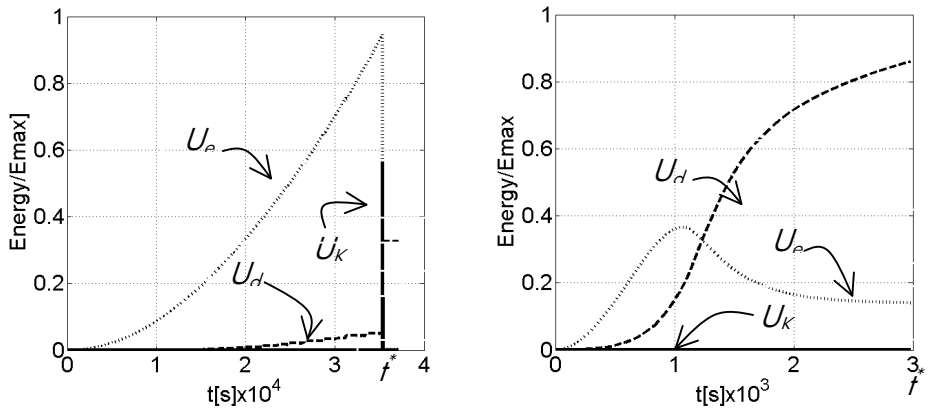

Figure 5.2. Energy balance vs time (U_e= elastic energy, U_k= kinetic energy, U_d= dissipated energy): (a) Uniaxial compression (E_{max}=4888Nm), (b) Three point bending (E_{max}=0.65Nm).

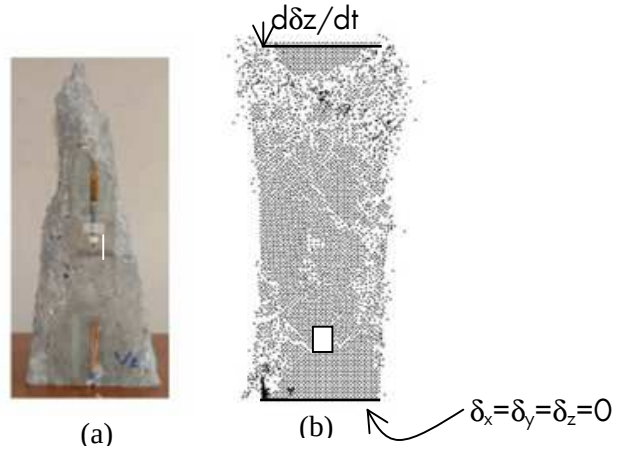

Figure 5.3. (a) Final rupture configuration of concrete specimen subjected to uniaxial compression (Carpinteri *et al*, 2009) and (b) collapse configuration predicted by DEM after peak load is reached. The white rectangle indicates the position of the sensor.

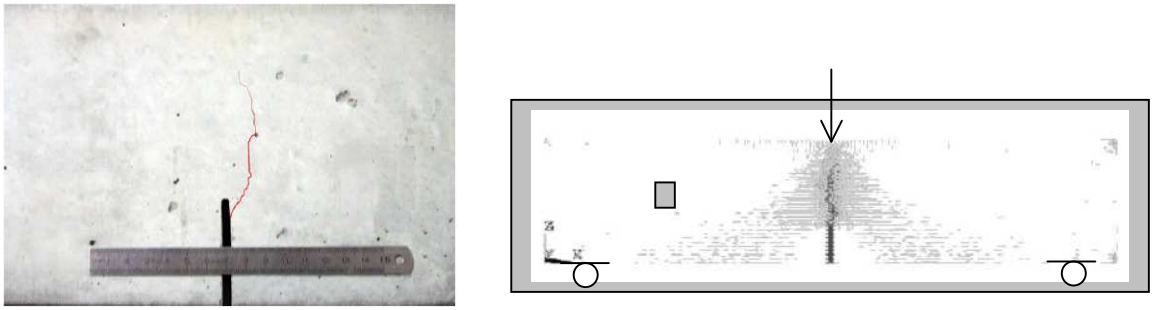

(a) (b)

Figure 5.4: (a) Experimental rupture configuration of specimen subjected to Three Point Bending (Carpinteri *et al*, 2009a) (b) Numerical rupture configuration according to DEM (only damaged bars are plotted). The small gray rectangle indicates the position of the sensor.

A summary of the numerical results concerning Acoustic Emission (*AE*) for both tests is presented next. *AE* signals in the numerical simulations are defined as the accelerations normal to the surface at points on the specimen where sensors were placed during the experiments. Figure 5.5 shows the occurrence of individual *AE* events as vertical bars on the time axis. The height of each bar is propotional to the intensity of the event registered on the sample surface. The figure also shows the total load vs. time curves. Histograms of the number of *AE* events and the evolution with time of the accumulated number of events are shown in Figure 5.6 for the uniaxial compression and for the three points bending tests. Finally Figure 5.7 shows the relations between the number of *AE* events and their magnitudes in logarithmic scale. Straight lines were fitted to the simulated data within selected time intervals, as indicated in the graphs. The magnitude scale was normalized. All the signals utilized for the *b*-values calculation in the numerical simulation had higher amplitudes than the fixed threshold A_{thres}. For this reason, only few events were identified in the simulation (about 200 in each example). By decreasing even further the displacement rate and adoting a lower threshold, it would be possible to identify more *AE* peaks, but the increase in computational time of the analysis was judged unnecessary. The values of *b* computed in both examples are compatible with the values determined experimentally by Carpinteri *et al* (2009, 2009b). In addition, the numerical simulations reproduced the tendency observed in laboratory experiments, which show that *b* decreases towards values around unity as the degree of damage increases. Note that in the uniaxial compression test the *b* value was observed to decrease from 1.69 to 1.19, while according to DEM predictions it decreases from 1.47 to 1.16. In the laboratory bending test, *b* decreases from 1.49 to 1.11, while the numerical simulation predicts a decrease from 1.10 to 1.03.

Finally Figure 5.8 presents plots of the logarithm of the number of events larger than given amplitudes vs. the logarithms of the amplitudes for DEM simulations of the compression test (left plot) and of the three points bending test (right plot). Notice that the shape of these curves are similar to the typical curve for seismic data shown in Fig. 4.1, which according to Scholz (2002), from the size distribution of subfaults, may be expected to present slopes given by $b_1 = \frac{2}{3}$ and $b_2 = 1$. While similar values are usually found in actual seismic records for specific faults or seismic regions, they differ from some of the laboratory or numerical simulation results for small samples discussed herein. For instance, equations (2.9) fitted to the data in Fig. 5.8, lead to $b_1 = 0.64$ and $b_2 = 2.40$ for the compression test and to $b_1 = 0.24$ and $b_2 = 1.16$ for the bending test.

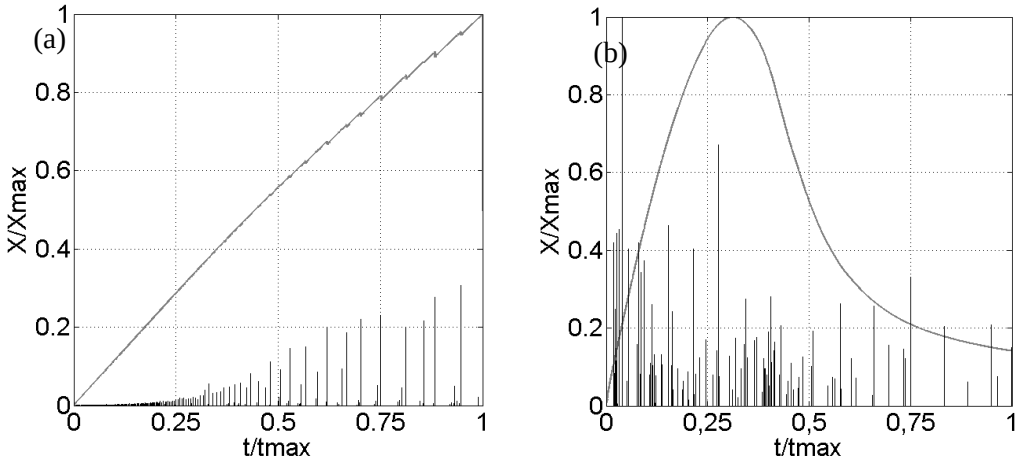

Figure 5.5. The full line curves indicate the total load in DEM models, while the bars show the amplitudes of *AE* events. Both axis were normalized to the maximum value. (a) uniaxial compression test, (b) Three points bending test.

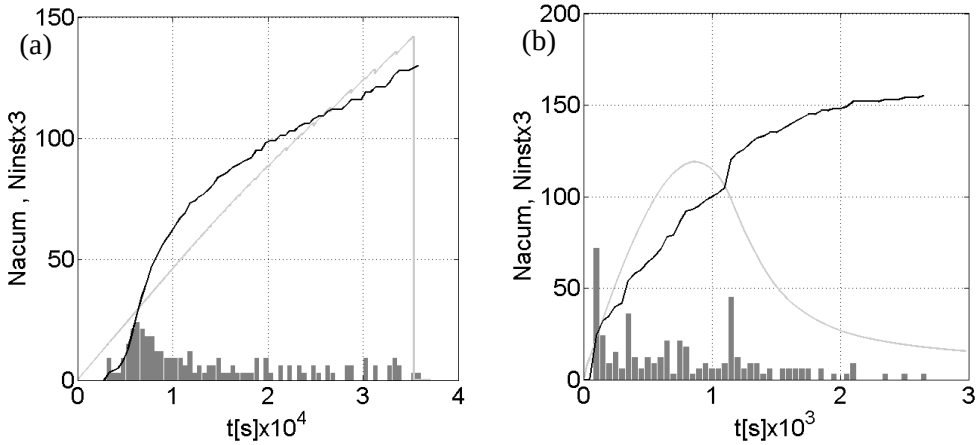

Figure 5.6. Histograms of the number of *AE* events and evolution with time of the accumulated number of *AE* events (thick line) and load evolution (thin line) for: (a) uniaxial compression test, (b) Three points bending test.

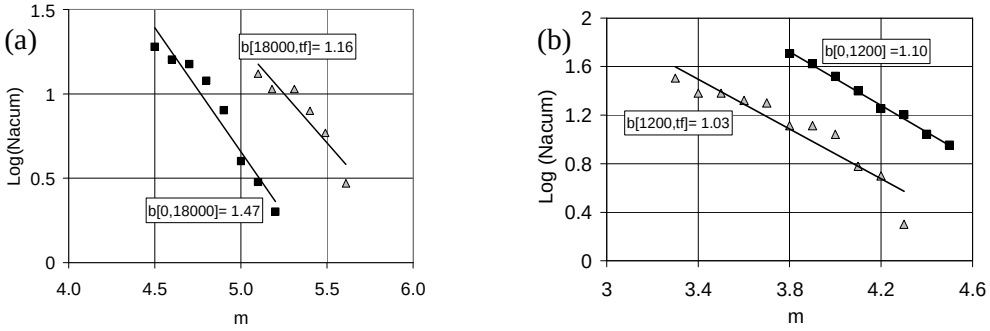

Figures 5.7. Determination of *b* - coefficients for simulated response in (a) uniaxial compression test and (b) three point bending test. The time intervals intervals used in the computation of *b* values are indicated between brackets.

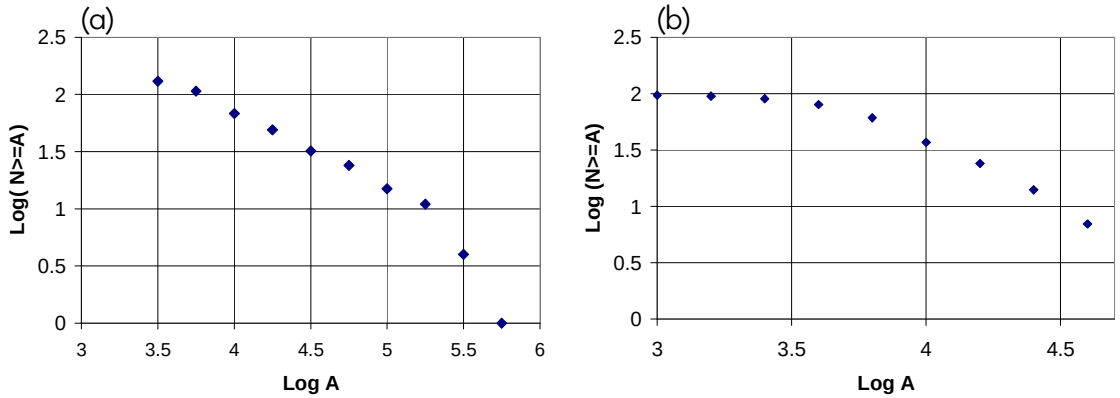

Figure 5.8: Logarithm of the number of events with amplitudes larger than A vs. logarithm of A for DEM simulations of compression (left) and of three points bending (right). The *b* values in the high magnitudes regions are b_2= 2.40 (compression) and b_2= 1.16 (bending).

6. CONCLUSIONS

The decrease of the slope *b* observed both in laboratory experiments on small samples, as well as in numerical simulations of these tests, which was interpreted as due to increasing damage in the medium, seems to contradict the usual shapes of seismic frequency vs. magnitude curves, shown by Figs. 2.1 (below) or 4.1, in which the slope *b* typically decreases as the magnitude increases. The latter, however, are plots of the *collected data* for the available time of observation, while the former refer to successive *periods of observation*. This is clearly illustrated by Figure 5.8, which presents results of the simulations of both the compression and bending tests reported herein, which are also characterized by slopes (*b* values) that decrease with magnitude.

A direct consequence of the previous observations would be that if seismic records for events at a given fault or well defined seismic region were separated in bins, say 500 years long, fits of the *GR* relation (2.1) to the separated data *should* present *b* values that decrease with time, that is, higher values for the older bins. Although this may be a generally valid rule, the differences for the final *b* values observed in the numerical simulations for large magnitudes suggest that b_2= 1 *may not* constitute the limiting slope in every case.

Another difficulty in comparisons of actual seismic data with laboratory or numerical simulation results is related to the manner in which foreshocks and aftershocks are considered in the elaboration of seismic catalogues. Note that in laboratory or numerical simulations, every *AE* event is counted, without any attempt to identify clusters of events. It has been noticed, moreover, that *AE* signals of large magnitude events do actually mask the simultaneous occurrence of smaller events (originated at different sources) triggered by the former.

These results suggest that some features of the probability distributions of earthquake magnitudes may be correlated with the evolution of the damage process for the source under consideration and that these features may be assessed using numerical models currently under development.

ACKNOWLEDGEMENTS

The authors acknowledge the support of CNPq and CAPES, Brazil.

REFERENCES

Abe, K. (1975): "Reliable estimation of the seimic moment of large earthquakes", *J. Physiks Earth Planet. Int.*, **23**, p. 381-390.

Bak, P. and Tang, C. (1989): "Earthquakes as a self-organized physical phenomenon", *Journal of Geophysical Research*, **94**, 15635-15637.

Bommer, J.J. and Stafford, P.J. (2008): "Seismic hazard and earthquake actions". *In*: *Seismic Design of Buildings to Eurocode 8*, A.Y. Elghazouli *ed*., Taylor and Francis, 6-46.

Carpinteri, A., Lacidogna, G, Puzzi, S.(2009): "From criticality to final collapse: evolution of the *b*-value from 1.5 to 1.0". *Chaos, Solitons and Fractals*, **41**, 843–853.

Carpinteri, A., Lacidogna G., Niccolini G. (2009): "Fractal analysis of damage detected in concrete structural elements under loading". *Chaos, Solitons and Fractals*, **42**, 2047–2056.

Cornell, C.A. and Vanmarcke, E.H. (1969): "The major influences on seismic risk", *Proceedings of the Fourth World Conference on Earthquake Engineering*, Santiago de Chile, Vol. 1, A-1, 69-93.

Esteva, L. (1976): "Seismicity" , Chapter 7, in *Seismic Risk in Engineering Decisions*, Edited by C. Lomnitz and E. Rosenbluth, Elsevier Scientific Publications, London.

Gutenberg, B. and Richter, C.F. (1954): "Seismicity of the Earth and Associataed Phenomena", Princeton University Press, Princeton, NJ, USA.

Hanks, T.C. and Kanamorri, H. (1979): "A moment magnitude scale", *Journal of Geophysical Research*, **84**, 2348-2352.

Ito, K. and Matsuzaki, M. (1990): "Earthquakes as self-organized critical phenomena", *Journal of Geophysical Research*, **95**, (B5) 6853-6860.

Kanamori, H. and Anderson, D.L. (1975): "Theoretical bases of some empirical relations in Seismology", *Bulletin of the Seismological Society of America*, *BSSA*, **65**, No. 5, pp. 1073, 1095.

Kosteski L., Iturrioz I., Batista R.G., Cisilino A. P.*:* "The truss-like discrete element method in fracture and damage mechanics*". Engineering Computations, 2011; 6: 765–787.*

Marzocchi, W. and L. Sandri (2003): "A review and new insigths on the estimation of the *b*-value and its uncertainty", *Annals of Geophysics*, **46**, No. 6, pp. 1271-1282.

Riera J. D.: "Local effects in impact problems on concrete structures". *Proceedings*, Conference on Structural Analysis and Design of Nuclear Power Plants, Porto Alegre, RS, Brasil, 1984; Vol. 3,CDU 264.04:621.311.2:621.039.

Scholz C. H. (1968): "The frequency- Magnitude Relation of Microfracturing in rock and its relation to earthquakes". Bull of the Seism. Soc of America, Vol 58 n1 pp399-415.

Scholz, C.H. (2002). The Mechanics of Earthquakes and Faulting, 2nd. Edition, Cambridge University Press

Schwartz, D.P. and K.J. Coppersmith (1984). "Fault behavior and characteristic earthquakes - examples from the Wasatch and San-Andreas fault zones". *Journal of Geophysical Research*, **89**, 5681-5698.

Wesnousky, S.G. (1994): "The Gutenberg-Richter or characteristic earthquake distribution, which is it?", *Bulletin of the Seismological Society of America-BSSA*, **84** (6), 1940-1959.

Youngs, R.R. and Coppersmith, K.J. (1985): "Implications of fault slip rates and earthquake recurrence models to probabilistic seismic hazard estimates". *Bulletin of the Seismological Society of America - BSSA*, **75**, 939-964.